



Aluminum particle reactivity as a function of alumina shell structure: Amorphous versus crystalline

Renita K. Walzel^a, Valery I. Levitas^b, Michelle L. Pantoya^{a,*}

^a Mechanical Engineering Department, Texas Tech University, Lubbock, TX 79409, USA

^b Departments of Aerospace Engineering and Mechanical Engineering, Iowa State University and Ames Laboratory, Division of Materials Science and Engineering, Ames, IA 50011, USA

ARTICLE INFO

Article history:

Received 8 August 2019

Received in revised form 13 December 2019

Accepted 28 June 2020

Available online 03 July 2020

Keywords:

Flame speed

Melt dispersion mechanism

Thermite

Aluminum

Diffusion reactions

Fluorination reactions

ABSTRACT

The objective of this study was to investigate Al particle reactivity as a function of the Al₂O₃ shell phase. Aluminum particles were thermally treated to transition the shell from amorphous to crystalline and each powder was combined with polytetrafluoroethylene (PTFE). Flame speeds were measured for Al + PTFE powder mixtures for two Al particle sizes that differ from micrometer (μAl) to nanometer (nAl) diameter and for both crystalline and amorphous Al₂O₃ shells encapsulating Al core particles. Results showed that μAl particles were more sensitive to shell phase than nAl particles. Reactions were modeled according to the melt dispersion mechanism (MDM), and altering the shell phase reduced the thickness, damaged the shell structure, impeded melt dispersion, and reduced flame speed for μAl particles by 45% and nAl particles by 12%.

© 2020 Elsevier B.V. All rights reserved.

1. Introduction

Aluminum (Al) powder is a commonly used fuel in pyrotechnic, explosive, and propellant formulations due to its high (85 GJ/m³) stored chemical energy. When Al particles are less than 25 μm diameter, the method of powder synthesis is often based on high temperature heating and evaporation of bulk Al [1,2]. As bulk Al is vaporized, it nucleates and condenses into an aerosol of molten droplets. The aerosolized droplets are cooled in an inert gas environment until solidified. At temperatures approaching ambient, a controlled oxygen concentration is introduced into the inert gas environment to form an amorphous oxide shell on the surface of the Al particles. The amorphous aluminum oxide (Al₂O₃) shell is thermodynamically stable with an amorphous to crystalline transition temperature of 440 °C [3–6]. The amorphous Al₂O₃ shell passivates the pyrophoric core and is roughly 4 nm thick regardless of particle size. Therefore, nano-aluminum (nAl) particles have a smaller percentage of active Al and more Al₂O₃ per weight and volume compared to micron-aluminum (μAl) particles.

The μAl combustion mechanism has been described in terms of mass diffusion through the Al₂O₃ shell, such that Al particle size influences overall reactivity. Because nAl particles have a higher surface area to volume ratio, in thermite there is more interface contact between fuel and oxidizer that reduces mass diffusion distances and promotes diffusion reactions compared with μAl particles. Osborne et al. [7]

examined nAl and polytetrafluoroethylene (PTFE) nanoparticle reactions using Differential Scanning Calorimetry (DSC). They showed an exothermic pre-ignition reaction (PIR) for nAl + PTFE that was not detectable for μAl + PTFE [7]. The increased exothermic energy associated with the PIR was attributed to higher interface contact between the Al₂O₃ shell surrounding nAl particles and PTFE [8]. The PIR energy was from a reaction between fluorinated fragments from decomposing PTFE and the Al₂O₃ surface, and was measured at heating rates on the order of 1 K/s. Energy from the PIR promoted higher exothermic energy in the main Al reaction but also facilitated decomposition of the fluoropolymer [9,10]. On average, nAl particles release three times more energy than μAl particles owing to the particle size difference.

Under equilibrium conditions (i.e., heating rates on the order of 1 K/s or less), the reaction mechanism for Al particles is based on shell growth as core aluminum oxidizes [11]. The growth of the Al₂O₃ shell surrounding the core Al has been described in four distinct stages by Trunov et al. [11] and illustrated in Fig. 1. In *Stage I* the amorphous shell increases in size but does not exceed a thickness of 4 nm. *Stage II* begins at about 440 °C in a pure oxygen environment where the amorphous shell transitions to crystalline γ-Al₂O₃. The γ-Al₂O₃ shell has a lower density (3.14 g/cm³) than the amorphous shell (3.65 g/cm³) and contracts around the core particle. Once shell transition occurs, γ-Al₂O₃ covers the Al core with a jagged morphology containing a surface structure represented by valleys and peaks. *Stage III* corresponds to growth of γ-Al₂O₃ from Al core reactions with the surroundings and the shell transitions through the intermediate steps γ → δ → θ to α-Al₂O₃ (transition

* Corresponding author.

E-mail address: michelle.pantoya@ttu.edu (M.L. Pantoya).

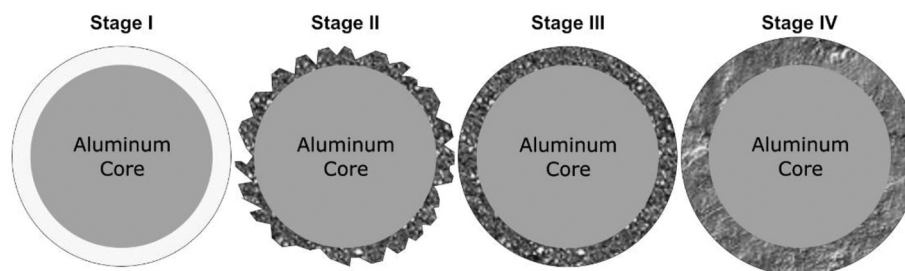


Fig. 1. Stage I–IV of shell growth on Al particles: Stage I the shell is amorphous Al_2O_3 , Stage II the shell transitions to $\gamma\text{-Al}_2\text{O}_3$ and has rough surface structure, Stage III the $\gamma\text{-Al}_2\text{O}_3$ shell grows and fills in gaps, and Stage IV the $\gamma\text{-Al}_2\text{O}_3$ shell transitions into $\alpha\text{-Al}_2\text{O}_3$ and continues to grow.

temperature $\sim 1025\text{ }^\circ\text{C}$). In Stage IV the shell is entirely $\alpha\text{-Al}_2\text{O}_3$ at roughly $1050\text{ }^\circ\text{C}$ and continues to grow up to 30 nm [11,12].

Under non-equilibrium conditions, nAl reactions proceed at a higher heating rate, on the order of 10^6 K/s , and via a different mechanism. One mechanism proposed by Levitas et al. [13,14] describes the heightened reactivity of nAl particles based on the mechanics of the core-shell particle structure and is applicable at high heating rates (i.e., $>10^6\text{ K/s}$). The model is diffusion-based but not reliant on shell growth or diffusion through the shell. When the Al core melts there is a 6% increase in molten core volume and as core volume expands, the Al_2O_3 shell is under tremendous hoop stress that eventually leads to shell failure and spallation. With the shell removed from the core, an unbalanced pressure causes propagation of the tensile pressure wave to the particle center and liquid cavitation of the core and dispersion of aerosolized molten Al droplets. The small droplets react faster without the shell barrier to hinder diffusion. The model is called the melt dispersion mechanism (MDM) because the core melts, disperses molten droplets, and reactions ensue without the constraints of the Al_2O_3 barrier. Therefore, if MDM is activated, the PIR may not occur at relevant time scales such that molten Al oxidation reactions may not be influenced by Al_2O_3 exothermic reactions.

The MDM is a mechanochemistry based model that determines reactivity as a function of the ratio of the Al particle core radius (R) to Al_2O_3 shell thickness (δ), such that the ratio M is R/δ . Levitas et al. [13–15] showed that MDM is optimized if $M < 19$, because the core becomes fully molten prior to shell spallation such that dispersion of a molten spray of droplets can be optimized. For Al particle mixtures, a heating rate greater than 10^6 K/s corresponds to a flame speed of approximately 10 m/s or larger. Also, for heating rates in excess of 10^6 K/s , MDM was found consistent with experiments for μAl particles less than $5\text{ }\mu\text{m}$ diameter [14–16].

The goal of the current work is to optimize Al particle reactivity in terms of increased reaction propagation. The objective is to examine the effect of shell phase on Al particle reactivity with PTFE. The hypothesis is that if MDM is activated, the PIR observed at heating rates of 1 K/s may not contribute energy that would increase flame speeds for reactions that occur at 10^6 K/s . A second objective is to extend this reactivity analysis to two different Al particle sizes in order to examine differences in reaction mechanisms that may also influence reaction propagation. The objectives are accomplished through flame speed measurements for both μAl and nAl powder combined with PTFE. The experiments are designed to establish limitations of the energetic contribution of the PIR and the role reaction mechanism plays in advancing energy propagation.

2. Experimental section

2.1. Materials: preparation and characterization

Two different Al powders were used that differ by their average particle diameter. The 80 nm average diameter Al particles (nAl) were supplied by NovaCentrix (Austin, TX) with an active Al concentration of

71 wt\% and $29\text{ wt\% Al}_2\text{O}_3$. The $1.5\text{ }\mu\text{m}$ average diameter aluminum particles (μAl) were supplied by Alpha Aesar (Tewksbury, MA) with a purity of 98% . Both suppliers characterized particle size and/or shell thickness using a transmission electron microscope (TEM), dynamic light scattering (DLS) and single-particle optical sensing (SPOS) instruments. The average initial shell thickness for both powders is 4 nm .

Spherical particles with $10\text{ }\mu\text{m}$ average diameter polytetrafluoroethylene (PTFE), Zonyl MP 1400, was supplied by DuPont® (Wilmington, DE) with a purity of 99% , a bulk density of 425 g/L , and a melting temperature of $325\text{ }^\circ\text{C}$ [17]. Powder PTFE was selected for this study because previous thermal analysis showed a PIR and main reaction with Al particles [7,17]. Different chain lengths of PTFE can exhibit variable PIR and main reaction behavior with Al particles in thermal analysis studies. For example, Mulamba et al. [17] studied the same PTFE powder used here (MP 1400) combined with nAl and found that the PIR and main reaction energy were highest for this fluoropolymer compared with three other PTFE fluoropolymers from DuPont®. The MP 1400 PTFE fluoropolymer had the longest chain length possessing increased fluorine concentration that contributed to improved reactivity for the nAl + PTFE reactions [17].

Transitioning the Al_2O_3 shell was accomplished by heating the powder at a rate of $20\text{ }^\circ\text{C/min}$ in a Vulcan® Burnout (Ney®) Model 3–130 oven to $450\text{ }^\circ\text{C}$ and holding for 15 min in an air environment. The particles were then slow cooled to ambient conditions over a 24-h duration. Work by Gesner et al. [18] established this heating protocol specifically to transition the shell phase without shell growth resulting in Stage II of the aluminum shell growth process (Fig. 1) [11]. Shell crystallization to $\gamma\text{-Al}_2\text{O}_3$ was confirmed through X-ray diffraction (XRD) analysis shown in Fig. 2A and B. A fully automated Rigaku Ultima III Powder XRD with incorporated cross beam optics (CBO) was used to analyze the powder samples for shell crystalline phase. The PXRD system was setup in parallel beam geometry and the data was collected in $2\theta/\theta$ mode to show that $\gamma\text{-Al}_2\text{O}_3$ is detected for both the nAl and μAl . The peaks for nAl are more easily detected for $\gamma\text{-Al}_2\text{O}_3$ because there is a higher percentage of Al_2O_3 per gram of powder as compared to μAl .

Aluminum particles with crystalline or amorphous shells were combined with PTFE at a mixture ratio of 55 wt\% PTFE and 45 wt\% of active Al content and maintained constant for all samples studied. This mixture ratio corresponds to an equivalence ratio (ER) of 1.7 (i.e. fuel rich). The balanced stoichiometric reaction is the same as used in previous work [17] and does not include the contribution of the PIR but assumes complete combustion of the Al and is shown in Eq. (1).



The powders were suspended in a polar carrier fluid, isopropanol. The solid to liquid ratio was maintained at 1000 mg:80 mL and contained in a 120 mL vial. The slurry was sonicated using a Misonix Sonicor 3000 (Farmingdale, NY) to break up agglomerates and allow homogeneous mixing. The sonicator was programmed for 10 s on/off cycle to prevent heating, and this cyclic program was applied for a total of 4 min . The mixture was then poured into a Pyrex™ dish and

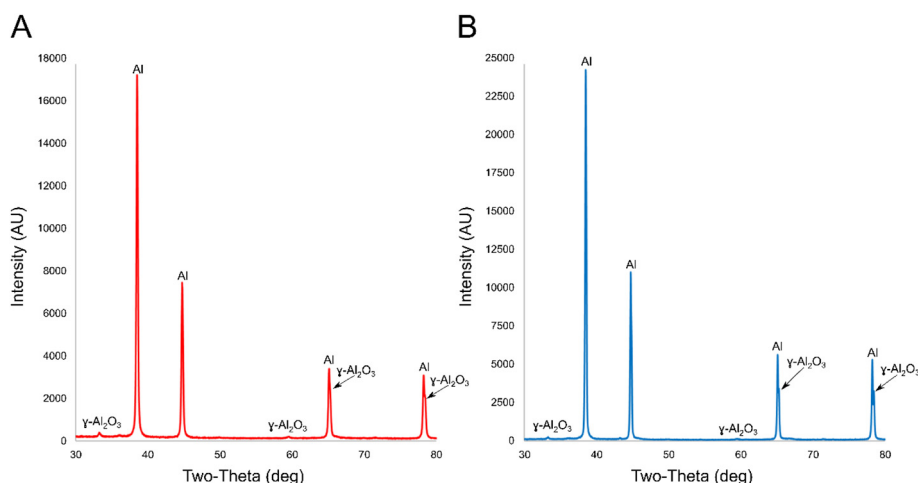


Fig. 2. Aluminum X-Ray diffraction results showing γ - Al_2O_3 for A) nAl and B) μAl .

dried in a chamber under ambient conditions for 48 h to evaporate isopropanol. The powder mixture was reclaimed with a grounded razor and sieved through 325 wire mesh for homogeneity in further experimentation.

Scanning electron microscopy (SEM) images of μAl + PTFE powder mixtures were captured with ZEISS GeminiSEM 450 with Gemini 2 optics. These images were used to analyze morphological differences between samples with different shell phases for μAl . Transmission electron microscopy (TEM) images of nAl particles were captured with a Hitachi H-9500 transition electron microscope. These images were analyzed to identify variations in shell structure associated with phase transition for nAl particles.

2.2. Reactivity characterization

About 350 mg of nAl + PTFE or 450 mg of μAl + PTFE powder were loaded into a quartz tube for flame speed measurements. The quartz tubes were durable and maintained structural integrity until the reaction front reached the end of the tube, allowing visualization of the reaction. The inner diameter of each tube was 3 mm and 10 cm in length. Data collection begins after the first 3 cm to account for entry effects that can cause unsteady propagation. The Al + PTFE powder was loaded into the flame tube by first measuring the amount of powder needed for the specified bulk density. The powder was separated into small batches and each batch was then loaded through a funnel connected to the quartz tube and compacted by tapping to facilitate settling of powder into the tube. This method was shown to avoid density gradients [19] that can produce high standard deviations between flame speed measurements.

The bulk density was measured in terms of percent Theoretical Maximum Density (%TMD). The TMD was calculated using Eq. (2) and %TMD in Eq. (3).

$$TMD = \frac{1}{\sum_i \left(\text{Mass}\%(i) * \frac{1}{\text{Density}(i)} \right)} \quad (2)$$

$$\%TMD = (\rho_{\text{mixture}}/TMD)*100 \quad (3)$$

Eq. (2) sums the i^{th} products of mass percent and specific volume of each reactant in the mixture. The summation of this product is necessary because the percentages of material are based on the mass of each component in the system. Density is a volume-based measure, but the percentages of material are mass-based. It is thus necessary to use specific volume (a mass-based unit) in lieu of density in the product

summation. The result of the summation is therefore a mass-weighted average of specific volumes (a mass-based unit). This result is then inverted to return density, which is a theoretical maximum for the mixture because it assumes no void spacing and only solid components consume the volume. This assumption is valid because the densities used in the calculation are bulk densities for each reactant. The density of the mixture (ρ_{mixture}) is determined from the mass of mixture divided by volume occupied, then divided by the TMD to provide the %TMD as in Eq. (3) and an indication of the bulk density of the mixture. The densities used in these calculations for amorphous Al_2O_3 and γ - Al_2O_3 are 3.14 g/cm^3 and 3.65 g/cm^3 , respectively and the density used for the PTFE was 2.2 g/cm^3 . Also, the calculation assumes 80 nm Al particles had 71 wt% active Al content and $1.5 \mu\text{m}$ Al particles had 98 wt% active Al content.

The powder was ignited through resistive heating of an Omega 24 AWG (0.51 mm) 80% Nickel / 20% Chromium (NiCr) hot-wire. The NiCr wire was inserted about 1.5 cm into the powder loaded tube and affixed with standard electrical tape. The NiCr hot-wire was attached to a 12 V DC power source and 30A was applied to the wire, resulting in resistive heating.

For each test, four tubes were prepared to assess repeatability of the measurements and determine standard deviation. The bulk density of μAl + PTFE was between 25 and 26%TMD and nAl + PTFE between 18 and 19%TMD, and both were kept constant to avoid differences in flame speed as a function of bulk density [20]. The nAl + PTFE has a lower bulk density because nAl particles have a higher surface energy (i.e., stronger van der Waal forces) and tend to resist compaction compared with their μAl counterparts [21].

Flame speed was determined by tracking the leading edge of light emitted during reaction propagation in a setup illustrated in Fig. 3. A Phantom v2512 high-speed camera recorded 1,100,000 frames per second (fps). The resolution of each recording was 1024×208 pixels and at this resolution each pixel was $9.01 \mu\text{m}$. A Nikon 105 mm 1:2.8D FX AF Micro-NIKKOR lens was applied to the camera and a HOYA 52 mm ND X2 50% neutral density filter was applied to the lens to prevent oversaturation of pixels during data collection. The camera was aligned perpendicular to the direction of flame propagation and through a viewing window into the testing chamber. The NiCr wire ignition source was connected to a firing trigger, which would initiate the reaction. Upon first light, the camera was triggered to record flame propagation. Each video was analyzed with a frame-by-frame tracking method from the Phantom camera software. This software allows the user to select the flame front and track its position as a function of time to determine flame speed.

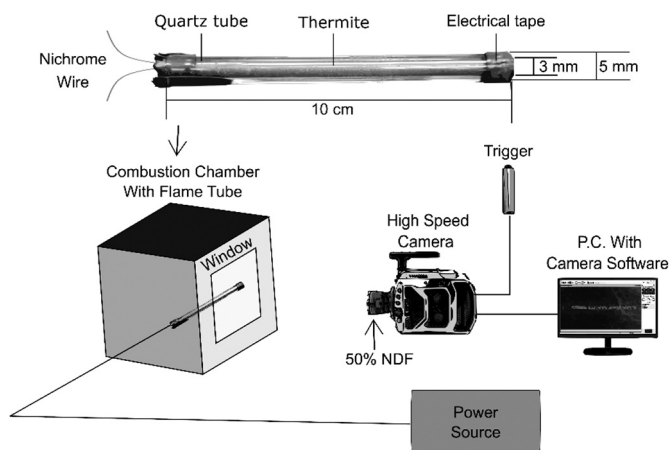


Fig. 3. Experimental setup for flame speed measurements. The powder is loaded into a tube that is positioned in the combustion chamber with a wire ignitor. The progression of the reaction is captured by a high-speed camera. The camera is positioned perpendicular to the direction of propagation.

3. Results

3.1. Material characterization

Fig. 4A and B illustrate shell phase does not appear to alter spherical particle morphology or cause differences in agglomeration. It is noted that due to the large difference in size, the PTFE is not pictured. Fig. 5 shows four images, the first corresponding to nAl particles with an amorphous Al_2O_3 shell (Fig. 5A). Particles of nAl that were thermally treated to transition the shell to a crystalline phase are shown in Fig. 5B and C. The more jagged edges of the shell are consistent with Stage II (see Fig. 1) but identifying crystallinity could not be achieved in the TEM analysis. Fig. 5D shows that some particles have a jagged fuller shell consistent with shell growth and transition to Stage III (see Fig. 1) but these were seldom seen unlike the particles in Fig. 5B and C.

3.2. Reactivity characterization

Flame speed measurements are shown in Table 1 and Fig. 6. The flame speeds in Table 1 are the average between four tests of each powder mixture but the scatter between each test is illustrated in Fig. 6 as a function of bulk density measured in terms of %TMD. Flame speeds are a function of %TMD such that due to the difference in %TMD between nAl and μAl , only the Al + PTFE flame speeds with the same Al particle size can be compared directly. It is noted that the largest standard deviation is for the μAl particles with crystalline shell and the larger deviation may be associated with variations in shell structure with size distribution for this powder.

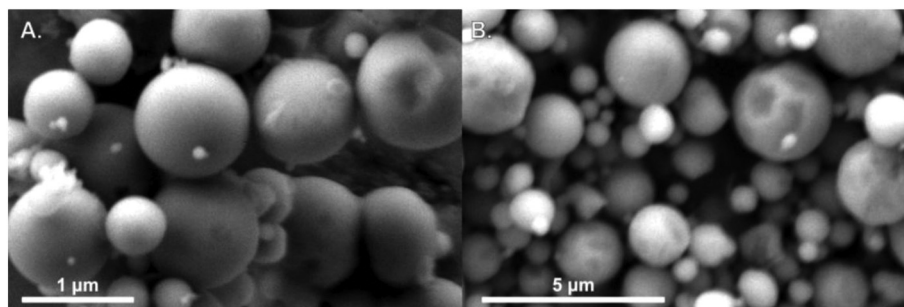


Fig. 4. SEM images of μAl particles. A) μAl with amorphous shell and a magnification of 13.24Kx and 5KeV. B) μAl with crystalline shell and a magnification of 3.67KX and 10KV. No difference in morphology is observed at this scale.

A representative sequence of select still frame images are shown in Fig. 7 to illustrate progression of the flame front, which is similar for all experiments. Due to the low bulk density of all Al + PTFE mixtures, the high rate of gas generation during reaction, and limited space for gas escape in the confined burning environment, convection is a dominant mode of heat transfer during flame propagation. While the leading edge of the flame front shows greater light intensity, lower light intensity is seen after flame front passage indicating continued deflagrating reactions occur behind the flame front.

3.3. Thermochemical equilibrium simulations

A thermochemical equilibrium simulation using NASA CEA [22] was performed to assess the influence of shell properties on combustion properties including adiabatic flame temperature and reaction pressure. The simulations were performed for the four Al + PTFE samples using constant volume conditions. Table 2 shows results for adiabatic flame temperature and pressure along with the corresponding average density of the mixture that varies as a function of shell concentration and phase. The heats of formation for amorphous Al_2O_3 and $\gamma\text{-Al}_2\text{O}_3$ are -1620 KJ/mol and -1656 KJ/mol, respectively [23]. The density used for each simulation was calculated using Eq. (2). Gas phase reaction products were 20 wt% for nAl reactions and slightly higher at 24% for μAl reactions. All mixtures included the following product species: AlF, AlF_3 , Al(l), Al_4C_3 (cr) as well as additional species in smaller concentrations (<0.1 mol fraction). The differences in gas phase product species can account for the difference in pressure between nAl and μAl reactions (Table 2), while the added Al_2O_3 concentration in nAl reactions provides a heat sink explaining the lower flame temperatures.

4. Discussion

Table 1 indicates that for nAl particles, there is just a 12% reduction in flame speed with Al_2O_3 shell phase. However, for μAl particles, transitioning the shell from amorphous to crystalline reduced the flame speed by 45%. The bulk densities between the two Al particle sizes are different enough (i.e., 18.75%TMD compared with 25.5%TMD) to preclude a flame speed comparison between the two particle sizes directly. But, the influence of shell phase for each Al size can be examined separately.

Thermal equilibrium simulations using NASA CEA (Table 2) show that μAl + PTFE has higher adiabatic flame temperature and pressure because this mixture has a lower concentration of Al_2O_3 compared with nAl + PTFE. The higher pressure and flame temperatures may aid energy transfer for μAl + PTFE. Despite the differences in thermal properties of amorphous compared with crystalline alumina, the adiabatic flame temperature and pressure do not change significantly for the same particle size (Table 2). Therefore, variations in shell structure do not affect thermal transport properties such that differences in

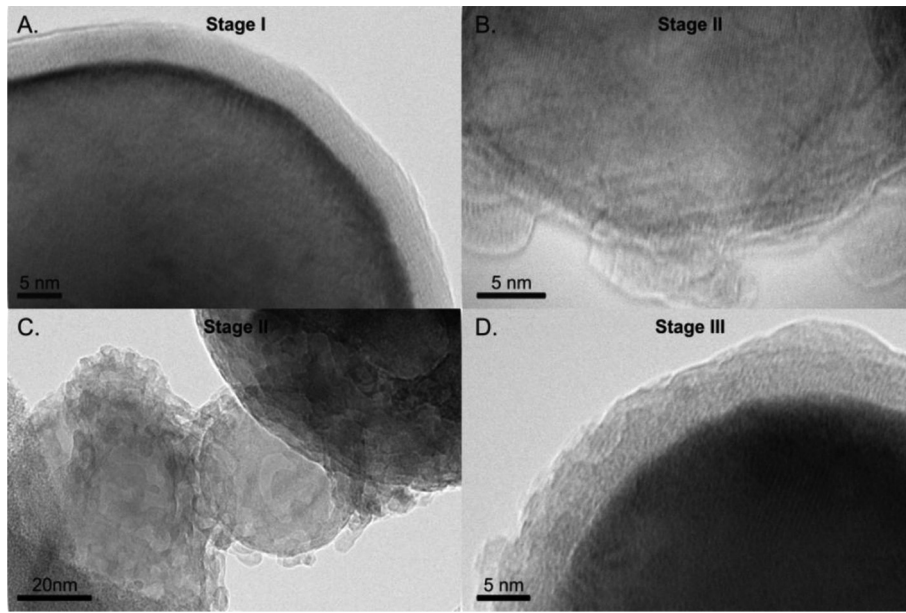


Fig. 5. TEM images of nAl particles. A) nAl with an amorphous shell taken at 300 KeV and a magnification of 700Kx. B) nAl with a crystalline shell taken at 300KeV and a magnification of 1500Kx, in Stage II of the oxidation process. C) nAl with a crystalline shell shown in (B) along with the surrounding particles also in Stage II, taken at 300KeV and a magnification of 200Kx. D) nAl particle with a crystalline shell and shell growth at Stage III of the oxidation process, taken at 300 KeV and 700Kx.

flame speed for the same particle size are linked with the mechanism for reaction rather than thermal mode for propagation.

For all cases in Fig. 6, the flame speed exceeds 10 m/s (i.e., and the heating rate exceeds 10^6 K/s), such that the MDM may apply for both Al particle sizes [24]. Previous work showed that the flame speed for nAl particles is the same for an amorphous and crystalline alumina shell [16,25] such that the crystalline alumina shell has approximately the same strength as the amorphous shell. Defects in alumina at the nanoscale produce smaller stress concentrations than in the bulk because defects are close to the free surface where stresses are inherently zero. For this reason, defective and irregular structure in the crystalline alumina shell does not significantly reduce the shell strength, but reduce shell thickness. The thickness of a crystalline shell is defined as the minimum thickness of the ring which does not have notches, i.e., δ_c is 2.4 nm from TEM analysis as in Fig. 5B. All irregularities in the shell increase thickness, and since they do not produce essential stress concentrators, the irregularities are not considered. In Pantoya et al. [20], the Al_2O_3 shell surrounding the Al particle was damaged by mechanically pressing powders to consolidate them to a higher bulk density. Even with the damaged shells, the flame speed for nAl and μAl particles was consistent with MDM. Damaged shells heal with time in an air environment and shell width increases in an air environment, as evidenced by comparison between Figs. 5B and D.

For Al particles reacting by MDM mechanism, the flame speed, V , can be expressed by Eq. (4) in terms of maximum flame velocity V_{max} .

$$V = V_{max} f = V_{max} \left(-B + \left(B^2 - 4AC \right) \right) / (2A) \text{ for } 0 < f < 1; \text{ and } V = V_{max} \text{ for } f = 1 \quad (4)$$

In Eq. (4), the volume fraction of melt within the core prior to shell spallation is f , and this volume fraction then disperses and participates in reaction within the flame front [13,15]. The equations for A , B , and C in Eq. (4) are given by Levitas et al. [13,15] and depend on the ratio

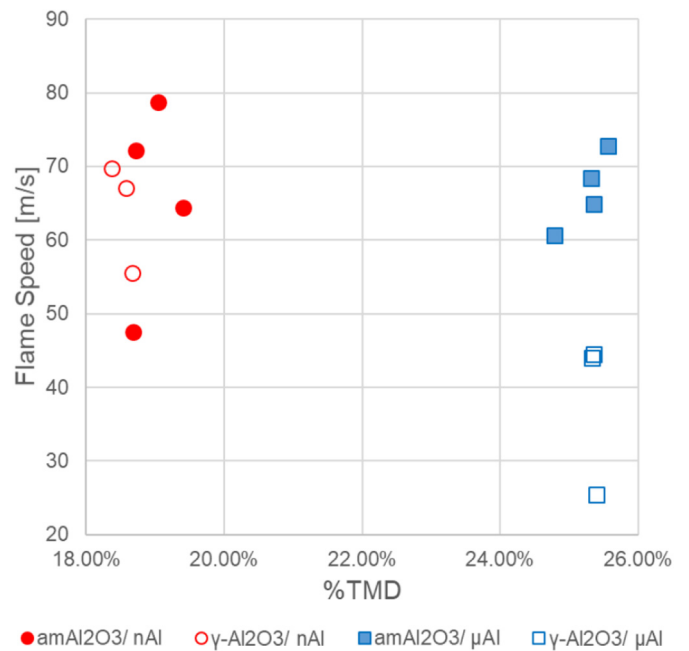


Fig. 6. Flame speed as a function of bulk density in terms of %TMD for nAl + PTFE (red symbols) and μAl + PTFE (blue symbols). The notation: am Al_2O_3 indicates an amorphous shell (open symbols) while $\gamma\text{-Al}_2\text{O}_3$ is the crystalline shell (closed symbols). (For interpretation of the references to colour in this figure legend, the reader is referred to the web version of this article.)

Table 1
Flame speeds for Al + PTFE reactions of varied Al particle sizes and shell phases.

Shell Phase	Avg. Al Particle Diameter (nm)	Bulk Density (%TMD)	Flame Speed (m/s)	Standard Deviation (m/s)
Amorphous	80	18.96	71.78	7.16
Crystalline	80	18.59	64.13	7.51
Amorphous	1500	25.25	67.26	6.13
Crystalline	1500	25.69	46.30	10.90

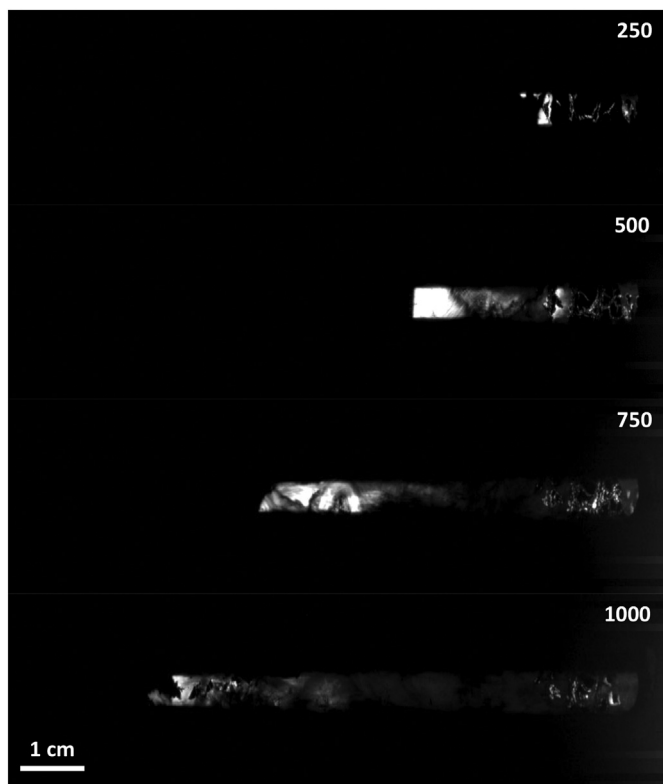


Fig. 7. A representative series of select still frame images showing the flame front for nAl with an amorphous shell + PTFE. The time stamp is in units of μ s from ignition.

(M) of Al core radius R to oxide shell thickness δ , $M = R/\delta$ and properties of Al and Al_2O_3 . For μAl particles M is large and Eq. (4) simplifies to Eq. (5).

$$V/V_{\max} = f = -1.052 + 0.103 \sigma_u + 0.001127T_o \quad (5)$$

In Eq. (5), σ_u is the strength of the shell in tension and T_o is the temperature at which the oxide shell is stress free. Here, $T_o = 300$ K. Note that Eq. (5) is independent of M and δ .

For μAl particles, R is 746 nm, δ_a is 4 nm, and δ_c is 2.4 nm, such that $M_a = R/\delta = 187$ and $M_c = 311$, i.e., M is large and Eq. (5) is applicable. For a shell with the ideal ultimate strength, $\sigma_u = 11.33 \text{ GPa}^{14}$, Eq. (5) gives $f = 0.453$. For μAl particles the flame speed is reduced by a factor of 1.45 (i.e., 67.26/46.3 from Table 1 and Fig. 6), and $f = 0.453/1.45 = 0.31$. If the reduction in flame speed is due to reduction in ultimate strength of the shell only, then with $f = 0.31$ in Eq. (5), $\sigma_u = 9.96 \text{ GPa}$. This is a realistic number that unhealed damage within 2.4 nm thick shell reduces its strength by 12% and therefore we assume the same σ_u for nAl.

For nAl particles, the particle core radius (R) is 36 nm, the amorphous shell thickness (δ_a) is 4 nm (Fig. 5a), and the minimum thickness of the crystalline shell (δ_c) is 2.4 nm (Fig. 5b). Therefore, for the

amorphous shell, $M_a = 9$, and for the crystalline shell, $M_c = 15$, both are smaller than $M = 19$ such that for ideal shell strength ($\sigma_u = 11.33 \text{ GPa}$), $f = 1$ and both nAl particles should be completely dispersed as molten aerosolized droplets above the melting temperature, regardless of shell phase. However, for $R = 36 \text{ nm}$, $\delta_c = 2.4 \text{ nm}$ (i.e., $M_c = 15$), and reduced strength $\sigma_u = 9.96 \text{ GPa}$ substituted into Eq. (4) instead, $f = 0.90$. The ratio of flame speed according to melt volume fraction is 1.11 (i.e., 1.0/0.9), which is in agreement to the experimental ratio of 71.78/64.13 = 1.12 (Fig. 6). Thus, for the M and δ ranges for nAl particles in these experiments, the nAl particles are less sensitive to damage and shell irregularities than μAl particles.

If reactions were diffusion controlled (or even if reactive sintering was considered), then the jagged shell morphology apparent in the crystalline shell structures of Fig. 5 would be far more reactive than the thicker, pristine shell barrier of the amorphous shelled particles. But, that is not observed, and the crystalline shell reduce flame speed for nAl (slightly) and μAl (more pronounced) particles.

5. Conclusions

Flame speeds were measured for mixtures of aluminum (Al) and polytetrafluoroethylene (PTFE) powders confined in tubes. Two Al particle diameters were investigated: 80 nm Al (nAl) and 1.5 μm Al (μAl) and two different shell structures were also investigated: amorphous and gamma phase Al_2O_3 . Flame speeds of Al + PTFE varied significantly for μAl particles based on Al_2O_3 shell phase, while nAl particles showed a small variation in flame speed as a function of Al_2O_3 shell phase. All Al particle reactions are consistent with the melt dispersion mechanism (MDM). Crystallization of the shell reduces thickness of the shell from 4 nm to 2.4 nm and the strength of the shell from 11.33 to 9.96 GPa. According to MDM theory, shell crystallization reduces flame speed for μAl by 45% and nAl by 12%, in good agreement with experiments. The crystalline shell reduced the measured flame speed because less of the core becomes molten prior to shell spallation such that accessibility of the molten aluminum to oxidizer is the speed limiting criteria. This study showed that activation of a reaction mechanism had more influence on the rate of energy propagation than surface exothermic reactions measured under equilibrium conditions.

Author contributions

The manuscript was written through contributions of all authors. All authors have given approval to the final version of the manuscript. The authors contributed equally.

Funding sources

Army Research Office award W911NF-17-1-0387; Office of Naval Research N00014-19-1-2082.

Declaration of Competing Interest

The authors declare none.

Acknowledgements

The authors RW and MP are grateful for support from the Army Research Office under award W911NF-17-1-0387 and our Program Manager, Dr. Ralph Anthenien. The authors MP and VL are grateful for support from Office of Naval Research under award N00014-19-1-2082 and our program managers, Dr. Chad Stoltz and Mr. Matthew Beyard. All authors are thankful for assistance from Dr. Julius Warzywoda for TEM analysis and Dr. Bo Zhao for help with SEM images, both at Texas Tech University.

Table 2

Summary of NASA CEA simulation results; Am is amorphous shell and γ is crystalline shell on Al particle.

Sample	Density (g/cm^3)	Flame Temperature ($^{\circ}\text{C}$)	Reaction Pressure (MPa)
Am nAl + PTFE	0.477	1972	56.4
γ nAl + PTFE	0.572	1956	55.2
Am μAl + PTFE	0.644	2292	69.0
γ μAl + PTFE	0.648	2296	69.4

References

- [1] S. Panda, S.E. Prantsinis, Modeling the synthesis of Aluminum particles by evaporation-condensation in an aerosol flow reactor, *Nanostruct. Mater.* 5 (1995) 755–767, [https://doi.org/10.1016/0965-9773\(95\)00292-M](https://doi.org/10.1016/0965-9773(95)00292-M).
- [2] S. Ozbilien, A. Unal, T. Sheppard, Influence of atomizing gases on the oxide-film morphology and thickness of Aluminum powders, *Oxid. Met.* 53 (2000) 1–22, <https://doi.org/10.1023/A:1004505728950>.
- [3] L. Jeurgens, W. Sloof, F. Tichelaar, E. Mittemeijer, Thermodynamic stability of amorphous oxide films on metals: application to aluminum oxide films on aluminum substrates, *Phys. Rev. B Condens. Matter Mater. Phys.* 62 (2000) 4707–4719, <https://doi.org/10.1103/PhysRevB.62.4707>.
- [4] D. Flötotto, Z.M. Wang, E.J. Mittemeijer, On the structural development during ultrathin amorphous Al₂O₃ film growth on Al(111) and Al(100) surfaces by thermal oxidation, *Surf. Sci.* 633 (2015) 1–7, <https://doi.org/10.1016/j.susc.2014.11.008>.
- [5] I. Levin, D. Brandon, Metastable alumina polymorphs: crystal structures and transition sequences, *J. Am. Ceram. Soc.* 81 (1998) 1995–2012, <https://doi.org/10.1111/j.1151-2916.1998.tb02581.x>.
- [6] L.P.H. Jeurgens, W.G. Sloof, F.D. Tichelaar, E.J. Mittemeijer, Growth kinetics and mechanisms of aluminum-oxide films formed by thermal oxidation of aluminum, *J. Appl. Phys.* 92 (3) (2002) 1649–1656, <https://doi.org/10.1111/j.1151-2916.1998.tb02581.x>.
- [7] D.T. Osborne, M.L. Pantoya, Effect of Al particle size on the thermal degradation of Al/teflon mixtures, *Combust. Sci. Technol.* 179 (2015) 1467–1480, <https://doi.org/10.1080/00102200601182333>.
- [8] M.L. Pantoya, S.W. Dean, The influence of alumina passivation on nano-Al/Teflon reactions, *Thermochim. Acta* 493 (2009) 109–110, <https://doi.org/10.1016/j.tca.2009.03.018>.
- [9] R. Padhye, A.J.A. Aquino, D. Tunega, M.L. Pantoya, Fluorination of an alumina surface: Modeling Aluminum-fluorine reaction mechanisms, *ACS Appl. Mater. Interfaces* 9 (28) (2017) 24290–24297, <https://doi.org/10.1021/acsami.7b05372>.
- [10] R. Padhye, D.K. Smith, C. Korzeniewski, M.L. Pantoya, Tailoring surface conditions for enhanced reactivity of aluminum powders with solid oxidizing agents, *Appl. Surf. Sci.* 402 (2017) 225–231, <https://doi.org/10.1016/j.apsusc.2017.01.016>.
- [11] M.A. Trunov, M. Schoenitz, X. Zhu, E.L. Dreizin, Effect of polymorphic phase transformations in Al₂O₃ film on oxidation kinetics of aluminum powders, *Combust. Flame* 140 (2005) 310–318, <https://doi.org/10.1016/j.combustflame.2004.10.010>.
- [12] E.N. Coker, The oxidation of aluminum at high temperature studied by thermogravimetric analysis and differential scanning calorimetry, *Sandia Rep. Sandia Natl. Lab.*, No. October 2013, pp. 1–22.
- [13] V.I. Levitas, M.L. Pantoya, B. Dikici, Melt dispersion versus diffusive oxidation mechanism for Aluminum nanoparticles: critical experiments and controlling parameters, *Appl. Phys. Lett.* 92 (2008) 1–4, <https://doi.org/10.1063/1.2824392>.
- [14] V.I. Levitas, B.W. Asay, S.F. Son, M.L. Pantoya, Mechanochemical mechanism for fast reaction of metastable intermolecular, *Methods* 101 (2007) 1–20, <https://doi.org/10.1063/1.2720182>.
- [15] V.I. Levitas, M.L. Pantoya, K.W. Watson, Melt-dispersion mechanism for fast reaction of aluminum particles: extension for micron scale particles and fluorination, *Appl. Phys. Lett.* 92 (2008) 5–8, <https://doi.org/10.1063/1.2936855>.
- [16] K.W. Watson, M.L. Pantoya, V.I. Levitas, Fast reactions with nano- and micrometer Aluminum: a study on oxidation versus fluorination, *Combust. Flame* 155 (2008) 619–634, <https://doi.org/10.1016/j.combustflame.2008.06.003>.
- [17] O. Mulamba, M.L. Pantoya, Exothermic surface chemistry on aluminum particles promoting reactivity, *Appl. Surf. Sci.* 315 (2014) 90–94, <https://doi.org/10.1016/j.apsusc.2014.07.112>.
- [18] J. Gesner, M.L. Pantoya, V.I. Levitas, Effect of oxide shell growth on nano-aluminum thermite propagation rates, *Combust. Flame* 159 (2012) 3448–3453, <https://doi.org/10.1016/j.combustflame.2012.06.002>.
- [19] E. Abdullah, D. Geldart, The use of bulk density measurements as a flowability, *Powder Technol.* 102 (1999) 151–165, [https://doi.org/10.1016/S0032-5910\(98\)00208-3](https://doi.org/10.1016/S0032-5910(98)00208-3).
- [20] M.L. Pantoya, V.I. Levitas, J.J. Granier, J.B. Henderson, The effect of bulk density on the reaction dynamics in nano and micron particulate thermites, *J. Propuls. Power* 25 (2009) 465, <https://doi.org/10.2514/1.36436>.
- [21] Y. Luo, R. Zhao, J.B. Pendry, Van der Waals interactions at the nanoscale: the effects of nonlocality, *Proc. Natl. Acad. Sci.* 111 (2014) 18422–18427, <https://doi.org/10.1073/pnas.1420551111>.
- [22] S. Gordon, B.J. McBride, Computer program for calculation of complex chemical equilibrium compositions and applications, Part 1: Analysis, Technical Report No. NASA-RP-1311, NASA Lewis Research Center, Cleveland, OH, USA, 1994.
- [23] M.W. Chase Jr., NIST-JANAF Thermochemical Tables, 4th ed. Part I. Al-Co American Institute of Physics, 1998 156–159.
- [24] V.I. Levitas, Burn time of aluminum nanoparticles: strong effect of the heating rate and melt dispersion mechanism, *Combust. Flame* 156 (2009) 543–546.
- [25] V.I. Levitas, Mechanochemical mechanism for reaction of aluminum nano- and micron-scale particles, *Phil. Trans. R. Soc. A* 371 (2013), 20120215.